ADVANCED FUNCTIONAL MATERIALS
www.afm-journal.de

Self-Established Rapid Magnesiation/De-Magnesiation Pathways in Binary Selenium–Copper Mixtures with Significantly Enhanced Mg-Ion Storage Reversibility

*Zhonghua Zhang, Bingbing Chen, Huimin Xu, Zili Cui, Shanmu Dong, Aobing Du, Jun Ma, Qingfu Wang, Xinhong Zhou, and Guanglei Cui**

Rechargeable magnesium/sulfur (Mg/S) and magnesium/selenium (Mg/Se) batteries are characterized by high energy density, inherent safety, and economical effectiveness, and therefore, are of great scientific and technological interest. However, elusive challenges, including the limited charge storage capacity, low Coulombic efficiency, and short cycle life, have been encountered due to the sluggish electrochemical kinetics and severe shuttles of ploysulfides (polyselenide). Taking selenium as model paradigm, a new and reliable Mg-Se chemistry is proposed through designing binary selenium-copper (Se-Cu) cathodes. An intriguing effect of Cu powders on the electrochemical reaction pathways of the active Se microparticles is revealed in a way of forming Cu_3Se_2 intermediates, which induces an unconventional yet reversible two-stage magnesiation mechanism: Mg-ions first insert into Cu_3Se_2 phases; in a second step Cu-ions in the $Mg_{2x}Cu_3Se_2$ lattice exchange with Mg-ions. As expected, binary Se-Cu electrodes show significantly improved reversibility and elongated cycle life. More bracingly, Se/C nanostructures fabricated by facile blade coating Se nanorodes onto copper foils exhibit high output power and capacity (696.0 mAh g^{-1} at 67.9 mA g^{-1}), which outperforms all previously reported Mg/Se batteries. This work envisions a facile and reliable strategy to achieve better reversibility and long-term durability of selenium (sulfur) electrodes.

1. Introduction

Rechargeable magnesium (Mg) batteries employing metallic Mg as anode are one of the candidates holding great promise to surpass Li-ion systems in the issues of energy density because of their two-electron redox property.[1,2] Besides, Mg metal possesses huge intrinsic advantages, including high safety (non-dendrite formation and less reactiveness at ambient atmosphere) and low cost benefitted from its natural abundance.[1–3] Unfortunately, the research of Mg batteries has received comparatively less attention owing to the absence of high-performance cathodes together with comprehensively well-performed Mg-ion electrolytes.

Until now, the most attractive system is still the first Mg battery prototype with more than 2000 cycles at 100% depth of discharge, which contains Chevrel phase cathode, Mg foil anode, and magnesium organohaloaluminate electrolyte.[4] It delivers a limited specific capacity ≈100 mAh g^{-1} and a relatively low operation voltage of ≈1.1 V versus Mg, making this Mg battery system energetically uncompetitive.[2,5] The conversion-type sulfur (S) and selenium (Se) cathodes, with theoretical volumetric capacity of 3467 mAh cm^{-3} for S and 3268 mAh cm^{-3} for Se, fulfill the criteria of high energy density, high safety, materials sustainability, and cost-effective features.[6–8] Nevertheless, researches on rechargeable Mg/S and Mg/Se battery systems are still in the nascent stage. With regard to selenium cathodes, there are only two reports recording their Mg-ion storage performances. Zhao-Karger et al. report that Se/CMK-3 electrode exhibits a high discharge capacity of 1689 mAh cm^{-3} yet a low capacity retention of ≈30% after 50 cycles.[8] Our previous work has demonstrated that the Se/C cathode displays stable capacity of ≈600 mAh g^{-1} in the initial cycle and achieves 60% capacity retention even after 200 cycles.

Previous studies suggest that the properties of Mg/S cells are severely hindered by the shuttles of polysulfide species and the sluggish conversion reactions from S to MgS (discharge process) due to sulfur's insulating nature.[5,9,10] These two aspects result in the overcharge behavior and low electrode utility, respectively. The large kinetic barriers during the recharge process of MgS also cause irreversibility and low Coulombic efficiency in all Mg/S cells, which is believed to be the major culprit for fast capacity fade.[5,10] Recently, Manthiram and Yu

Dr. Z. Zhang, Dr. B. Chen, Dr. Z. Cui, Dr. S. Dong, A. Du, Dr. J. Ma, Dr. Q. Wang, Prof. G. Cui
Qingdao Industrial Energy Storage Research Institute
Qingdao Institute of Bioenergy and Bioprocess Technology
Chinese Academy of Sciences
Qingdao 266101, P. R. China
E-mail: cuigl@qibebt.ac.cn
Dr. Z. Zhang, A. Du
University of Chinese Academy of Sciences
Beijing 100190, P. R. China
H. Xu, Prof. X. Zhou
College of Chemistry and Molecular Engineering
Qingdao University of Science and Technology
Qingdao 266042, P. R. China

DOI: 10.1002/adfm.201701718

present a Mg/S cell with a sandwich-structured cathode (pre-activated carbon nanofiber-sulfur-carbon nanofiber), exhibiting prolonged cycle life.[10] A "Li^+-ion mediation" strategy has also been reported by Wang and co-workers, which significantly improves the performance of the Mg/S cells.[5] The above progresses provide effective solutions to achieve high capacity of Mg/S cells. However, severe overcharge behavior and large voltage hysteresis during charge and discharge process still exist in these systems, leading to fast capacity fade. In these studies, sulfur cathodes can only be cycled less than 50 cycles even using carbon-encapsulating sulfur structures.

The sluggish recharge process of the electrochemically inactive discharged products (low-order $MgSe_x$ and/or MgSe species) and the severe shuttling effects of various polyselenides are also serious impediments to the development of Mg/Se batteries.[6,8] However, no modified Mg/Se cells have been reported so far in spite of the fact that Se-based cathodes are believed to show faster kinetics, higher electrode utilization, and better rate capability than the S-based cathodes due to selenium's higher electronic conductivity (≈20 orders of magnitude higher than that of S) and higher ionic conductivity of its discharged products.[6,11] In consideration of the high volumetric energy density of the redox-active Se/Mg couple, fundamentally viable engineering technologies are urgently needed for the development of practical Mg/Se cells.

In this work, we for the first time propose a facile and effective strategy enabling the microsized Se-based electrode with markedly improved Mg-ion storage reversibility and cyclic durability via introducing crude copper powders. A robust intermediate phase of Cu_3Se_2 has been formed during the initial discharging process, which activates the sluggish reaction between selenium and Mg^{2+} by acting as a thermodynamically stable phase inserting Mg-ions up to the composition range $0.1 \le x \le 0.5$ in $Mg_{2x}Cu_3Se_2$. During the next magnesiation stage, the reversible displacement reaction generates Cu nanowires and MgSe nanoparticles. The electro-induced copper products can effectively re-trap the polyselenides when the electrode is recharged. This unconventional yet reversible reaction has been revealed via density function theory (DFT) calculations accompanied by a series of ex situ X-ray power diffraction (XRD) patterns, X-ray photoelectron spectroscopy (XPS), scanning electron microscopy (SEM) images, energy-dispersive spectroscopy (EDS), and scanning transmission electron microscopy (STEM) images. The Se-Cu binary system exhibits much better electrochemical response compared with the pure selenium electrodes. Our work opens up a new window to achieve better reversibility and durability of selenium electrode for high energy density Mg batteries.

2. Results and Discussions

Although tailoring the materials' size and morphology has been proven to be a promising solution to achieve improved Li-ion and Mg-ion storage performances, microsized materials are much more favorable for practical battery applications because they often offer higher tap density and are expected to deliver higher volumetric energy density.[12,13] Only several cathodes, for example, Cheverel phase,[4] layered TiS_2,[14] thiospinel Ti_2S_4,[15] covellite CuS,[16] β-$CuSe_2$,[17] and $MgMSiO_4$ olivine compounds (M = Fe, Co, and Ni),[2] display reversible Mg-ion storage properties. In following sections, we show how the microsized and high-capacity selenium electrode exhibits highly reversible magnesiation/de-magnesiation properties along with largely elongated cycling stabilities.

As still at a nascent stage, no standard Mg-ion electrolytes and cell designs are available for Mg-Se batteries. Understanding the effects of varied electrolyte and current collectors on the electrochemical performances of Mg-Se batteries is highly critical for achieving optimized specific capacity, rate capability, and cycle life. Systematic investigations have been first conducted to reveal the underlying contributions of these battery components. As seen in **Figure 1**, Se-C composites (fabricated by melting Se powders into disordered mesoporous carbons) display varied electrochemical properties when using different electrolytes and current collectors. Specifically, when examined in boron-centered anion-based magnesium (BCM) electrolyte, Se-C@Cu electrode shows stable specific discharge capacity of 532, 502, 466, 426, 391, and 292 mAh g^{-1} at 50, 100, 200, 500, 1000, and 1250 mA g^{-1}, respectively. In a sharp contrast, when examined in hexamethyldisilazane (HMDS)-based electrolyte, although a high discharge capacity of 720 mAh g^{-1} is shown in the first cycle at a current density of 50 mA g^{-1}, the discharge capacities are dramatically decreased to 340 and 185 mAh g^{-1} at the 2nd and 20th cycles, respectively. Furthermore, the rate capability of Se-C@Cu‖HMDS‖Mg battery is much worse than that of Se-C@Cu‖BCM‖Mg battery as shown in Figure S1 (Supporting Information) and Figure 1b. More interestingly, both Se-C@GF‖BCM‖Mg battery and Se-C@Al‖BCM‖Mg battery show very poor electrochemical performances as demonstrated in Figure 1e,f, respectively. Figure S2 (Supporting Information) also illustrates the superior electrochemical response of Se-C@Cu‖BCM‖Mg battery compared to batteries using varied Mg-ion electrolytes including all phenyl complex (APC), magnesium-aluminum chloride complex (MACC), and HMDS-based electrolytes. These preliminary results reveal that both copper current collector and as-used BCM electrolyte may take part in the electrochemical reactions and contribute to the electrochemical data, highlighting the need for unraveling the underlying Mg-ion storage mechanisms.

2.1. Characterization of the Se-Cu Electrode

In order to rule out the effect of capacity contribution from disordered mesoporous carbons and excess amount of copper from current collectors, commercially available micrometer-sized selenium and copper powder (see Figure S3, Supporting Information) is directly used to prepare cathodes. Two types of Se-based electrodes have been first fabricated for high energy density of Mg/Se batteries. The pristine Se electrode is composed of Se powder, Super-P, and polytetrafluoroethylene (PTFE) binder with a weight ratio of 7:2:1, while the Se-Cu electrode comprises of 40 wt% Se powder, 40 wt% Cu powder, 10 wt% super-P, and 10 wt% PTFE binder. XRD patterns of both electrodes (Figure S3b, Supporting Information) indicate that the selenium powder composes of mixed hexagonal and monoclinic crystalline types and the Se-Cu electrode has a typical characteristic feature of Se and Cu mixed phases. It is

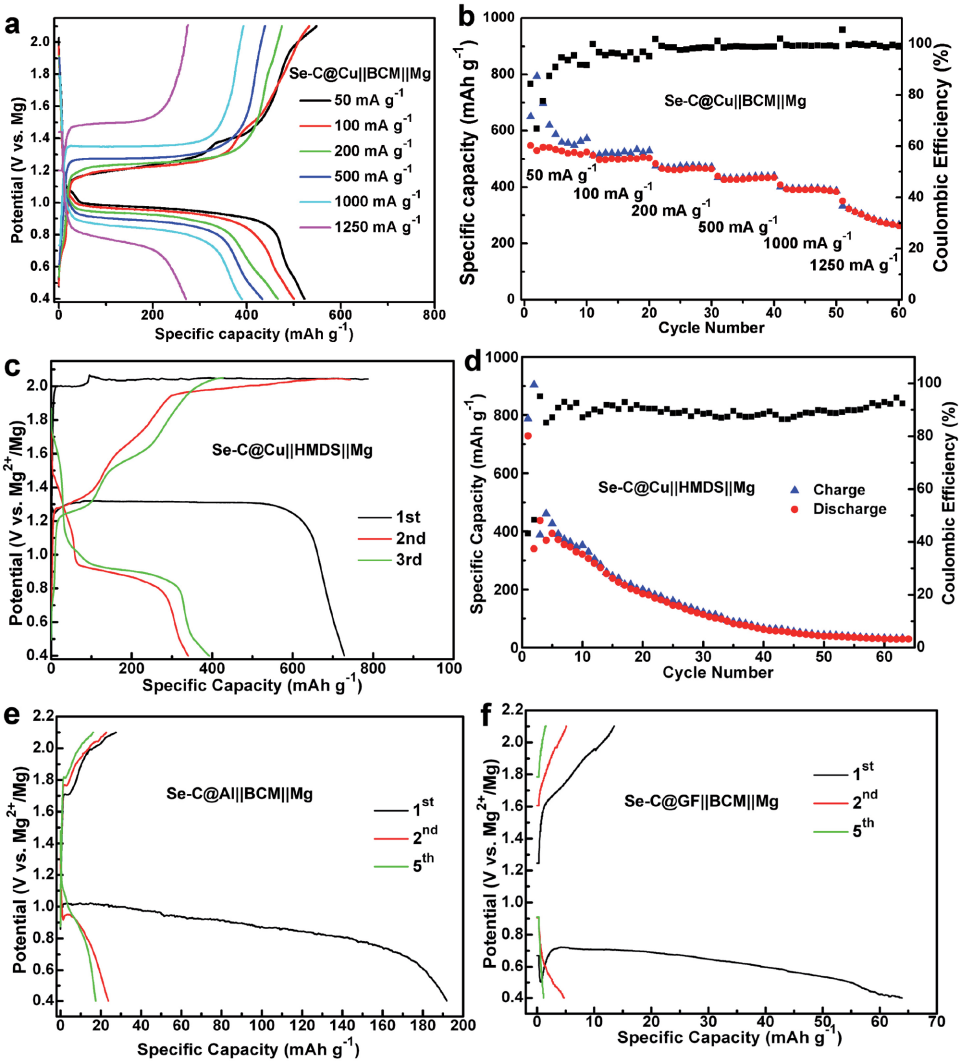

Figure 1. a,c) Galvanostatic charge/discharge profiles and b,d) the corresponding cycling performance of the Se-C@Cu electrode examined in various electrolyte: a,b) BCM electrolyte and c,d) HMDS-based electrolyte; galvanostatic charge/discharge profiles of e) Se-C@GF electrode and f) Se-C@Al electrode examined in BCM electrolyte.

worth noting that another phase (CuSe) appears during the fabrication of the Se-Cu electrode, which might be formed via the directly chemical reaction between copper and selenium when dried in vacuum oven at 120 °C. This result resembles the in situ chemical intercalation of Cu into Mo_6S_8 cathode when the Cu powder and Mo_6S_8 powder are mixed together for several hours.[18]

2.2. Electrochemical Performance of the Se-Cu Electrode

First, the Mg-ion storage properties are tested via cyclic voltammetry (CV) measurements using BCM electrolyte. Our previous explorations demonstrate that BCM electrolyte can meet the requirements of compatibility with both electrophilic selenium and metallic Mg anode.[19] The first cycle CV curve (**Figure 2**a) of the pristine Se electrode shows a couple of cathodic-anodic peaks, which is at around 1.9 and 0.8 V versus Mg, corresponding to the one-step de-magnesiation/magnesiation processes. In the second cycle, it displays a pair of redox peaks at 1.9 and 0.6 V versus Mg, indicating that large overpotentials exist during the discharging process. In contrast, the Se-Cu electrode (Figure 2b) exhibits much more discernable redox peaks, especially in the second CV cycle, which shows two pairs of cathodic and anodic peaks at about 1.2 V, 1.5 V versus Mg and 1.2 V, 0.8 V versus Mg, respectively. It is clear that the Se-Cu electrode delivers a multiple de-magnesiation/mechanism mechanism. The reduction peak of R1 and R2 also increases after the first CV cycle, indicating the enhanced charge storage capacity. In addition, compared to that of the pristine Se cathode, the Se-Cu electrode displays significantly reduced overpotentials of per redox pairs. These peaks identification and explanation are given in the following sections. From the cumulative reduction Coulombs in Figure 2c, the pristine Se electrode shows decreased capacity by ≈45% after the first cycle, while the Se+Cu electrode delivers enlarged capacity after

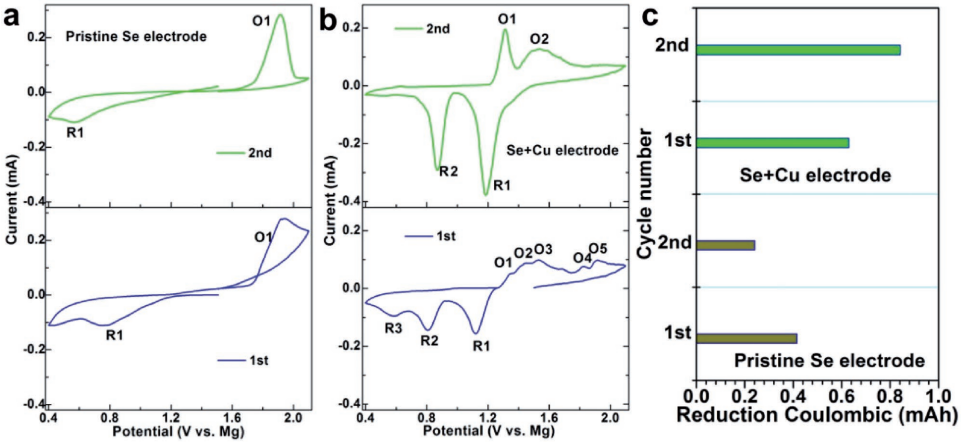

Figure 2. CV curves of the a) pristine Se electrode and b) Se-Cu electrode at a very low scan rate of 0.05 mV s^{-1}; c) The cumulative reduction Coulombs of both electrodes.

the first cycle by 20%. These results suggest that the introduction of Cu powder effectively improves the reversibility of the Se electrode.

The electrochemical reactivity of both the Se-Cu electrode and the pristine Se electrode is also evaluated by representative galvanostatic charge/discharge measurements as shown in **Figure 3**a,b. With regard to the Se-Cu electrode (Figure 3a), three obvious plateaus are observed in the first discharging curves at around 1.30, 1.22, and 0.95 V versus Mg, respectively, representing multistep magnesiation processes. The initial discharge capacity is up to 328 mAh g^{-1} based on the weight of active Se particles (164 mAh g^{-1} based on the total mass of Se and Cu), corresponding to ≈0.95 electrons (e^-) involved in charge transfer. During the charging processes, there are no obvious plateaus in the voltage range of 0.8–2.1 V versus Mg. In the subsequent cycles, the Se-Cu electrode displays two discharging plateaus at about 1.30 and 1.0 V versus Mg and two charging plateaus at 1.25 and 1.40 V versus Mg, respectively, which is highly consistent with the former CV curves (Figure 2). It should be noted that the reversible capacity is increasing from the first cycle onward to the tenth cycle, which reaches up to a maximum value of 408 mAh g^{-1} (204 mAh g^{-1} based on the total mass of Se and Cu), representing 1.2 e^- reaction involved in discharging process. In a sharp contrast, the pristine Se cathode (Figure 3b) displays a relatively low capacity of 262 mAh g^{-1} (≈0.77 e^- reaction) and one discharging

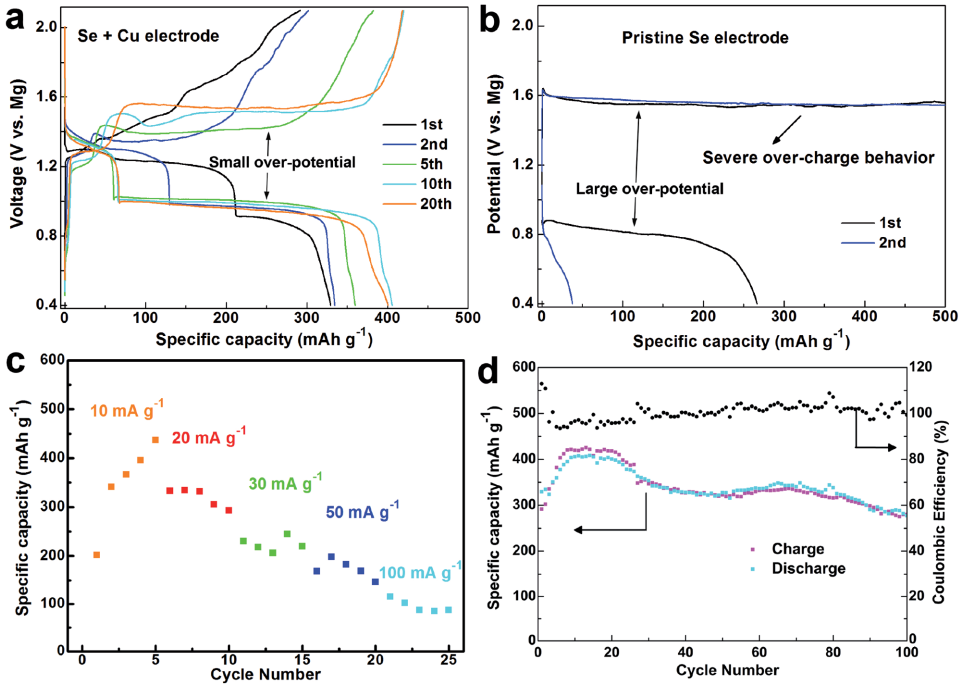

Figure 3. Galvanostatic charge/discharge profiles of the a) Se-Cu electrode and b) pristine Se electrode at a current density of 10 mA g^{-1}; c) Rate performance of the Se-Cu electrode; d) The cycling performance of the Se-Cu electrode at a constant current density of 10 mA g^{-1}.

plateau at ≈0.85 V versus Mg during the initial cycle. Severe over-charge behavior process is observed during the recharging process, mainly caused by the dissolution of polyselenides.[20–22] The second recharging profile of the pristine Se electrode displays similar over-charge behavior as that of the initial process and a sharply reduced discharging capacity of less than 50 mAh g^{-1} (only 0.14 e^- reaction) has been observed. In addition, the charge–discharge profiles of the pristine Se electrode show much larger overpotential compared to that of the Se-Cu electrode.

To clearly clarify the role of Cu in the electrode, the Se-Cu electrodes with different Se/Cu weight ratio (i.e., 1:0, 2:1, 1:1, and 1:2) have been prepared. For example, the Se-Cu electrode (with Se/Cu ratio of 2:1) comprises of 53 wt% Se powder, 27 wt% Cu powder, 10 wt% Super-P, and 10 wt% PTFE binders. Figure S4a (Supporting Information) shows the first galvanostatic charge/discharge profiles of the Se-Cu electrode with different Se/Cu weight ratios (2:1, 1:1, and 1:2). It is clear that Se-Cu electrode with Se/Cu ratio of 1:2 displays the largest specific capacity (based on the weight of Se) and a very flat voltage plateau at 0.9 V versus Mg. Se-Cu electrode with Se/Cu ratio of 1:1 displays a lower specific capacity of 218 mAh g^{-1} (based on the weight of Se powder), and two distinct voltage plateau at 1.18 and 0.9 V versus Mg. The Coulombic efficiency is dramatically improved when adding higher copper content in Se-Cu cathode. Figure S4b (Supporting Information) shows the typical galvanostatic charge/discharge profiles of the Se-Cu electrode with different Se/Cu weight ratios after several charge–discharge cycles. Se-Cu electrode with Se/Cu ratio of 1:2 delivers the largest specific capacity (based on the weight of Se powder) up to 660 mAh g^{-1} and a flat voltage plateau at 1.0 V versus Mg. It should be noted that similar voltage profiles have been observed for both Se-Cu electrodes with Se/Cu ratio of 1:1 and 2:1, which deliver improved electrochemical performances in terms of specific capacity and voltage polarization after 10th and 34th charge–discharge cycles, respectively. Figure S4c,d (Supporting Information) shows the corresponding cycling performance of three Se-Cu electrodes with specific capacities calculated based on the weight of Se and the total mass of Se and Cu, respectively.

A particular phenomenon that the reasonable electrochemical performances are obtained after continuous charge–discharge cycles has been observed for all three Se-Cu electrodes. Interestingly, Se-Cu electrodes with a higher Cu content need less charge–discharge cycles to reach their optimized specific capacity. A reasonable explanation for the increasing capacity during the first ten or so cycles might be caused by the slow penetration of electrolyte into the cathodes and the progressively improved wetting property. The gradually enhanced Mg stripping/plating properties of the as-used BCM electrolyte during the first tens of cycles are also responsible for the increasing capacity of Se-Cu electrodes as demonstrated by our previous work. It is obvious that Se-Cu electrode with Se/Cu ratio of 1:2 delivers the highest specific capacity based on the weight of only Se powders, while Se-Cu electrode with Se/Cu ratio of 2:1 delivers the highest specific capacity based on the total mass of Se and Cu. In summary, Se-Cu electrodes with different Se/Cu ratios show varied electrochemical properties in terms of specific capacity, voltage plateau, Coulombic efficiency, and cycle processes to achieve their optimized properties.

The rate performance of Se-Cu cathode is shown in Figure 3c and Figure S5 (Supporting Information). At a lower current density of 20 and 50 mA g^{-1}, the Se-Cu cathode delivers a specific capacity of 330 and 200 mAh g^{-1}, respectively. However, when the current density increases to 100 mA g^{-1}, it shows only 100 mAh g^{-1}, much lower than that of the Se-C@Cu electrode (Figure 1a,b).

The Se-Cu electrode displays improved cycling stability as seen in Figure 3d. After the 25th cycle, the capacity retention of the Se-Cu electrode remains to be 94.3%, whereas for the pristine Se electrode the capacity retention drastically decreases to 16.4% only after the second cycle. The long-term cycle test displays that the Se-Cu electrode shows a high capacity retention of 71.7% after 100 charge–discharge cycles, representing the best cyclic performance for the Se/Mg cells.[8,19] The Coulombic efficiencies in the Se-Cu cathode are calculated via 100 times the discharge capacitance divided by the charge capacity. During the first several cycles, more than 100% of Coulombic efficiency has been observed, which might be due to the sluggish electrochemical transformation of MgSe to Se species leading to imbalanced discharge/charge capacity. Superior Coulombic efficiency is also obtained for the Se-Cu electrode, which maintains at ≈100% as shown in Figure 3d. It should be noted that this work represents the first implementation of microsized Se powder for Mg batteries, which surpasses the Mg-ion storage properties of Se/CMK-3 electrodes[8] in terms of the electrode utilization and cycling stability. These all-above results manifest that the addition of Cu powder plays a crucial role in both activating the sluggish reaction between Se and Mg-ions and alleviating the shuttles of polyselenides.

Electrochemical impedance spectroscopy has been measured to check the impedance of Se-Cu electrode during various charge/discharge cycles (Figure S6, Supporting Information). With the capacity increasing, there is a significant decrease in the impedance after cycling, which can be attributed to the improved electrolyte penetration, the electrode wetting property, as well as the gradually enhanced electrochemical response of the as-used BCM electrolyte.

In order to achieve high output capacity, Se/C nanostructures have also been synthesized via a simple ball-milling process. As seen in **Figure 4**a, the Se/C nanostructures are composed of Se nanorodes with an average length of 80 nm and acetylene carbon nanoparticles (with a weight ratio of 25%). A high areal loading Se/C electrode (up to 2.0 mg cm^{-2}) was fabricated on Cu foil via facile blade-casting method. The modified Se/C electrode displays high specific capacity up to 459.1 mAh g^{-1} at 0.1 C (third cycle, here 1C = 679.0 mA g^{-1}), which increases to its highest value of 696.0 mAh g^{-1} at 34th cycle (Figure 4c). After 60 cycles, the modified Se/C electrode can still deliver 601.7 mAh g^{-1} at 0.1 C, demonstrating its excellent cycling performance. It should be noted that the modified Se/C electrode can be cycled at relatively high current density of 0.5 C, at which it displays 404 mAh g^{-1} at 60th cycle. The Se/C nanostructures can also be cycled at 1.0 C with a specific capacity of 160 mAh g^{-1}. It is clear that Se/C nanostructures deliver much higher specific capacity, rate performance, and lower voltage polarization compared to that of the Se-Cu electrode, which could be ascribed to the reduced Mg^{2+} diffusion pathways derived from the smaller particle size of Se

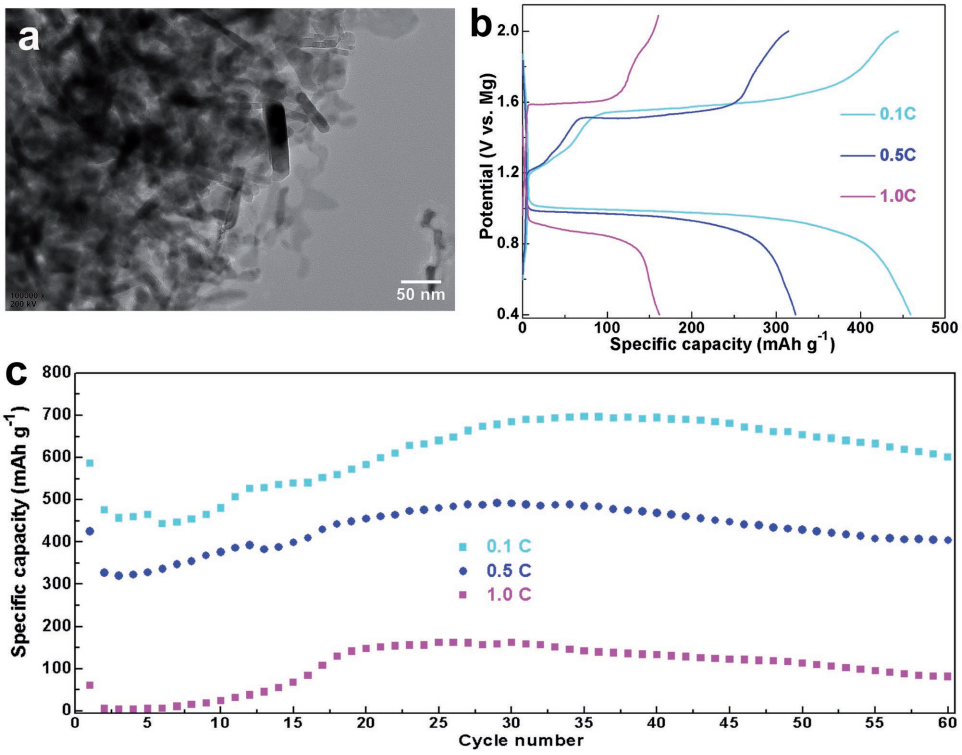

Figure 4. a) TEM image of the Se/C nanostructures; b) Galvanostatic charge/discharge profiles of the Se/C nanostructures at 0.1, 0.5, and 1.0 C; c) Cycling performance of the Se/C nanostructures.

nanorodes and the improved electronic conductivity attributed by acetylene carbons. The above results suggest that the Se/C nanostructures are potential to provide much higher output capacity and power.

The electrochemical performances of the Se/C nanostructure cathode without Cu foil have been tested in order to clearly clarify the critical contribution of Cu in accelerating the reaction kinetics of Se-based electrodes. As shown in Figure S7 (Supporting Information), the Se/C nanostructure cathode without Cu foil displays far inferior electrochemical response in respect of specific capacity, Coulombic efficiency, and cycling stability. These results also well agreed with the aforementioned discussions.

2.3. Ex Situ SEM, XRD, and XPS Investigations of the Se-Cu Electrode

In order to investigate the Mg-ion storage mechanism, seven key points have been selected to take XRD tests (**Figure 5**) during the first charge–discharge process. From the collected ex situ XRD patterns of the Se-Cu electrode at OCV and Point B, we confirm that a new phase of tetragonal-Cu_3Se_2 is dominantly observed, along with a trace of MgSe, Cu, and $Cu_{2-x}Se$ phases. This indicates that an in situ reaction between element Se and Cu preferably occurs during the first discharging step. Polyselenides (such as Mg-Se_8) may be first formed and subsequently dissolve into electrolyte to become a liquid cathode.[9,23] Liquid-polyselenides may react with Cu powders forming the stable Cu_3Se_2 species. Potentially, liquid-polyselenides are further reduced to lower-order polyselenides (e.g., from Se_8 to Se_4) during this discharging stage.[24,25] A trace of MgSe accompanied by the disappearance of Cu powders has also been observed. The XRD pattern at point C is similar to that of point B but shows much wider peak and slight peak shift toward high angles. In order to understand the magnesiation mechanism during this stage, the formation energy of Mg inserting in the Cu_3Se_2 has been discussed via DFT calculations. It has been known that the formation energy for per Mg is given as

$$E_f = \left[E_{Mg2\times Cu_3Se_2} - E_{Cu_3Se_2} - 2\times E_{Mg}\right] \quad (1)$$

where the $E_{Mg2\times Cu_3Se_2}$ is the total energy of the system containing 2× Mg atoms in the supercell, $E_{Cu_3Se_2}$ is the total energy of Cu_3Se_2 supercell, and E_{Mg} is taken as the energy of single Mg atoms, respectively. Compared with the different interstitial positions (Table S1, Supporting Information) for possible Mg intercalating, it is found that the S2 site may be the favorable position (Figure S8, Supporting Information). Therefore, in our work, we add the Mg atoms into the lattice to construct the Mg concentration x range ($0.1 \le x \le 1$) in $Mg_{2x}Cu_3Se_2$. Figure 5d–h shows the structure evolution when Mg ions are potentially inserted into the Cu_3Se_2. What's more, it is worth noting that the formation energy (Figure 5i) is kept at low value of –2.7 eV when the Mg concentration is lower than 0.5. However, the formation energy increases sharply as the Mg concentration increases. These results may suggest that there are two-stage magnesiation mechanism: (1) When x is between 0.1 and 0.5, intercalation of Mg-ions into Cu_3Se_2 intermediate phase is highly favorable; (2) In the next stage from $Mg_1Cu_3Se_2$ to

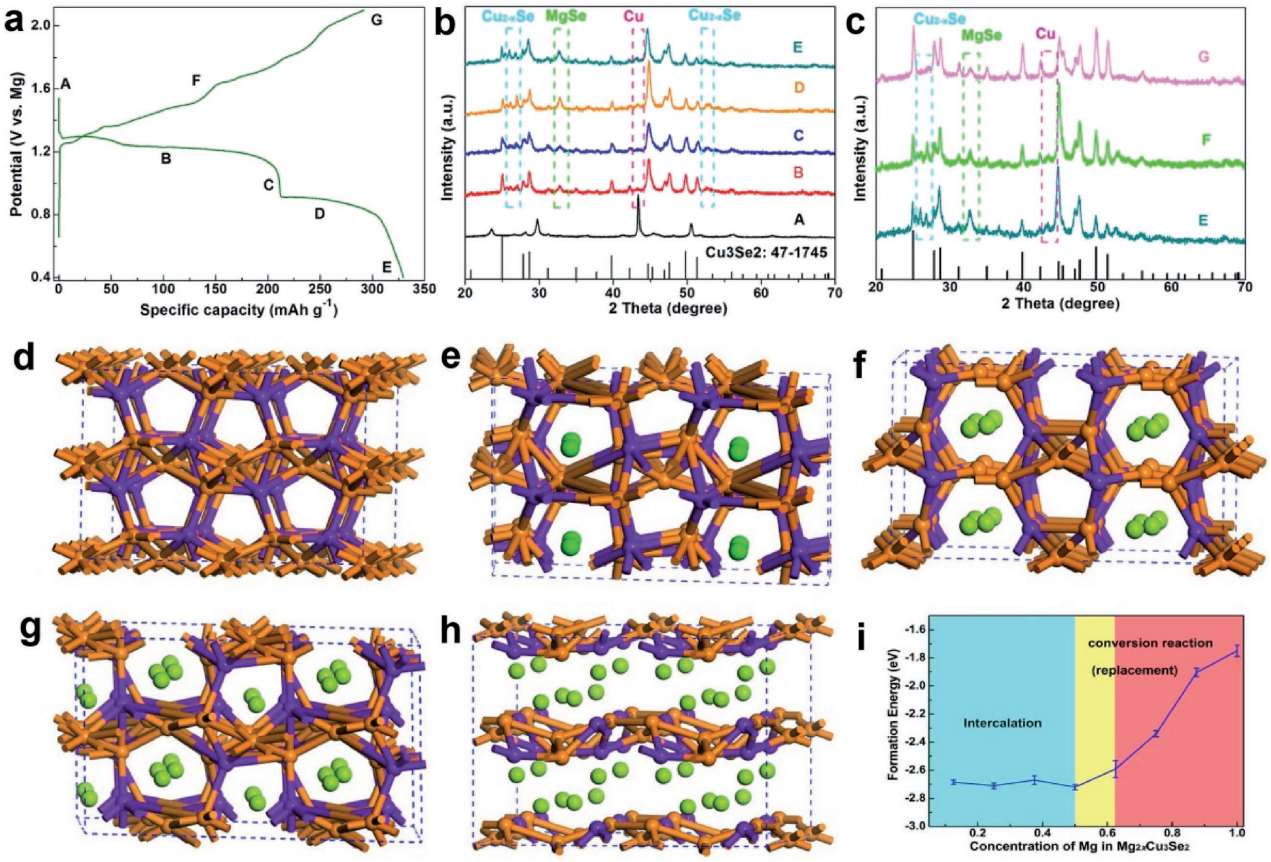

Figure 5. a) The first galvanostatic charge/discharge profiles of the Se-Cu electrode; The collected ex situ XRD patterns of the Se-Cu electrode: b) discharge process and c) recharge process; First-principles modeling on the two-step magnesiation of the Cu_3Se_2 intermediate phase: d) the crystal structure of Cu_3Se_2; the most favorable interstitial positions for Mg intercalation in e) $Mg_{0.25}Cu_3Se_2$, f) $Mg_{0.5}Cu_3Se_2$, g) $Mg_{0.75}Cu_3Se_2$, and h) $MgCu_3Se_2$ (yellow: Cu atom, purple: Se atom, green: Mg atom); i) The two-step magnesiation of Cu_3Se_2 evidence in the formation energy per Mg in $Mg_{2x}Cu_3Se_2$.

$Mg_2Cu_3Se_2$, that Cu_3Se_2 experiences conversion reactions due to the structural instability hinted by the sharply increased E_f value. The above first principles calculation results are also consistent with the discharged capacities at different states shown in Table S2 (Supporting Information).

In order to give direct proofs on the Mg-ion intercalation capability of Cu_3Se_2 intermediates, pure phases of Cu_3Se_2 and $Mg_{0.2}Cu_3Se_2$ have been synthesized by facile high-energy ball milling process. XRD patterns of both samples are shown in Figure S9 (Supporting Information). All the diffraction peaks can be well indexed to the tetragonal Cu_3Se_2 (PDF No. 71-0045). No other impurity peaks are observed from $Mg_{0.2}Cu_3Se_2$. The STEM images (b) and the corresponding elemental mapping images of the $Mg_{0.2}Cu_3Se_2$ can further demonstrate that the microsized particles are probably composed of Cu_3Se_2 and $Mg_xCu_3Se_2$, which share the same phase structure.

During the last discharging process (from point D to point E), the intensity of MgSe phase is greatly improved, together with the reappearance of the XRD patterns of Cu species, indicating a phase transfer occurring among Cu_3Se_2 and Mg-ions. The above results reveal that the Se-Cu electrodes undergo dramatic composite changes during the discharging process, which is highly consistent with the first principles calculation results. During the reverse process (from point E to point F and point G), XRD patterns discover the disappearance of Cu-characteristic peaks and the weakened MgSe peaks, suggesting a highly reversible reaction during the charge–discharge process. The main recharged products are determined to be Cu_3Se_2 with partial MgSe. To obtain an explicit reaction mechanism in our work, much more investigations including ex situ XPS and SEM analyses are discussed in the following sections.

Ex situ XPS has been conducted to gain a deeper understanding on the redox reactions occurring at the Se-Cu cathode. Mg-Se cells were disassembled at different discharged and charged stages for chemical analysis as seen in **Figure 6**. High-resolution Se 3d spectra obtained from the Se-Cu cathodes show that the one couple of characteristic peaks of Se 3d5/2 and 3d3/2 are located at 54.5 and 55.3 eV, which are consistent with selenium element (Se^0) according to previous reports.[6,22,26] After the initial discharge (magnesiation process) to point C, Se 3d5/2 and Se 3d3/2 peaks (Figure 6b) move toward lower binding energies: 54.2–55.0 eV. According to previous literatures, these binding energies belong to the Se 3d5/2 and 3d3/2 of diselenides (Se_2^{2-}) and polyselenides (Se_n^{2-} chains (n = 3, or 4)), respectively.[26–28] When the electrode is fully discharged (Point E), the binding energy peaks exhibit one broad peak at around 54.5 eV accompanied by a weak peak at 53.9 eV, which correspond to the Se 3d5/2 and 3d3/2 of Se_2^{2-} ions and

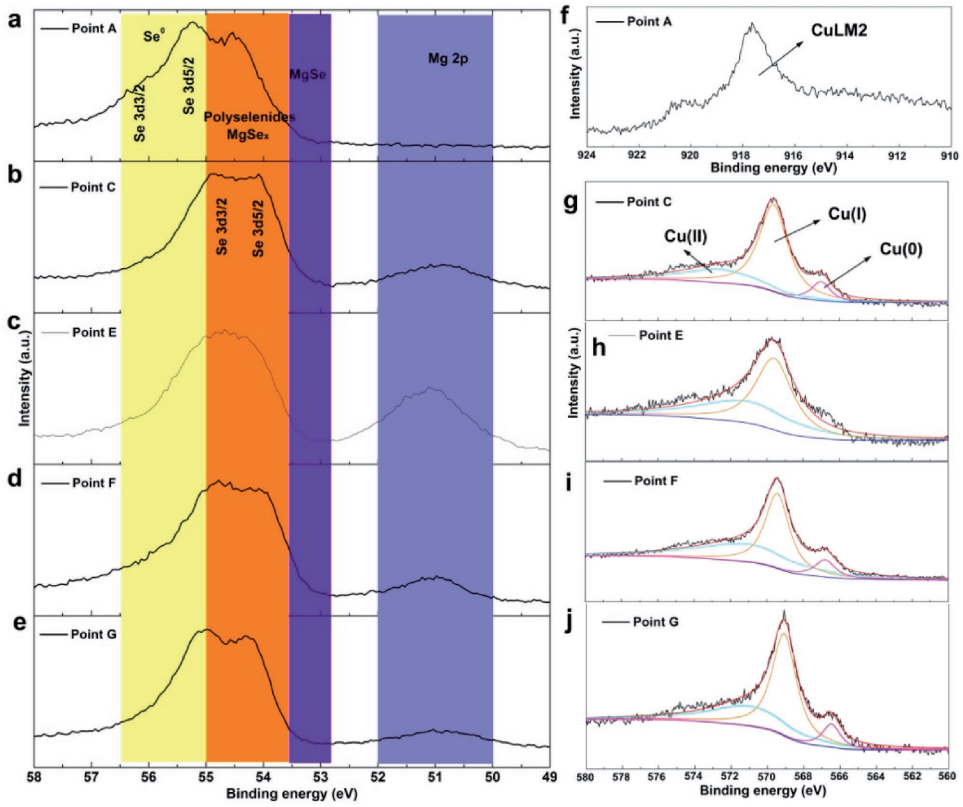

Figure 6. Selenium range XPS spectra of the Se-Cu electrode at various states: a) OCV, b) point C, c) point E, d) point F, and e) point G; Shift in kinetic energy of the CuLM2 Auger peak of the Se-Cu electrode at various states: f) OCV, g) point C, h) point E, i) point F, and j) point G.

Se^{2-} ions.[26] These results show clear evidence of multistep magnesiation mechanism during the discharge process and also a fully conversion reaction of Se elements (Se^0) to Se_2^{2-} and Se^{2-} ions. However, the utilization of selenium is incomplete, which is in accordance with the specific capacity results in Figure 3a and Table S2 (Supporting Information). After the Se-Cu electrode recharged to Point F and Point G, the Se 3d5/2 and Se3d3/2 peaks are shifted to higher binding energy accompanied by the sharp reduced intensity of Mg 2p peaks, indicating the reversible electrochemical insertion and conversion reactions related to the Cu_3Se_2 intermediates. In order to exactly understand the chemical states of Se in the charged Se-Cu electrode, high-resolution Se 3d XPS spectra have been provided as shown in Figure S10 (Supporting Information). A couple of Se 3d peaks at ≈54.7 eV (3d5/2) and ≈55.7 eV (3d3/2) with a spin–orbit splitting of 1.0 eV are consistent with that of Se(0), while Se 3d peaks at ≈53.9 eV (3d5/2) and ≈55.0 eV (3d3/2) can be ascribed to Se(II) species. Thus, the mole ratio of Se/Cu_3Se_2 in the discharged products can be approximately determined to be 2.

In addition, the Mg 2p peaks are detected at point C and point E discharge states, suggesting the possible formation of the MgSe and $MgSe_2$ as the final discharge products.[8,29] The intensity of Mg 2p peak at fully discharge state (point E) is enhanced compared to that at partially discharged state (point C), indicating much more completed conversion from Se^0 to MgSe (XRD results show the MgSe peaks rather than $MgSe_2$). It should be noted that the Mg 2p peaks do not disappear completely, which suggests the less electrochemically activity of MgSe species as that of MgS species.[5] This might also contribute to the capacity fade in the subsequent cycles as that occurs in Mg-S systems.[9,21,30]

Copper addition plays a pivotal role in activating the sluggish reaction between Mg^{2+} and Se element in the Se-Cu electrode. First, the solubility of Cu(I) or Cu(II) species has been authenticated by EDS data of the cycled Mg anodes as shown in Figure S11 (Supporting Information). Surprisingly, no Se-based species are detected in the cycled Mg anodes, suggesting the suppressed shuttle effects of Se-Cu electrode. It is difficult to clearly differentiate the Cu(I) and Cu(0) species based on the Cu2p core peak (see Figure S12, Supporting Information). The Cu LM2 Auger peaks have been investigated as shown in Figure 6f–i because they are more sensitive to the changes of chemical state compared to the Cu 2p XPS peaks.[31,32] The Cu LM2 peak at point A has a kinetic energy of 917.65 eV corresponding to Cu(0) according to previous reports.[33] No lower kinetic energy is detected for the Cu(I) in range of 916.5 ± 0.5 eV. For the partially discharged product at point C, the Cu LM2 peak displays two peaks at binding energy of 567.11 and 569.79 eV, which can be ascribed to Cu(0) and Cu(I), respectively.[32,33] The Cu LM2 peak completely shifts to around 570.00 eV and partially 571 eV at the fully discharged states indicating a fully conversion from Cu(0) to Cu(I) and Cu(II). At the reverse charged states (point F and point G), the Cu LM2 peak reversibly shifts to lower binding energy of ≈566.5 and ≈569.0 eV, suggesting the reformation of metallic Cu species

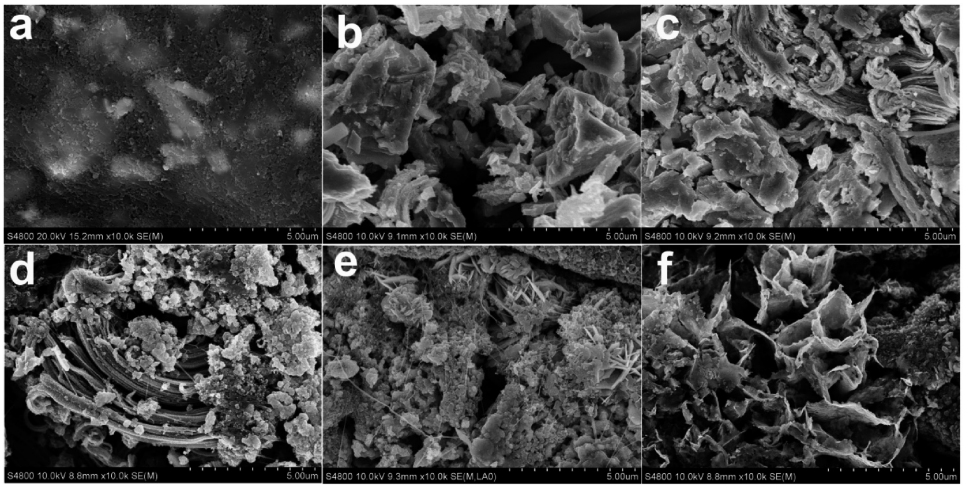

Figure 7. SEM images of the Se-Cu electrode in different charge–discharge states: a) OCV, (b) discharged to point B, c) discharged to point D, d) discharged to point E, e) recharged to point F, and f) recharged to point G.

in the recharge process. All above XPS analysis provides strong evidence on the astonishing effects of added Cu powders on the conversion reaction between Se element and MgSe discharged products. We also conclude that the initially formed intermediate Cu_3Se_2 species play a crucial role in the discharged (magnesiation) process while the reformation of metallic Cu may also function on the recharged (demagnesiation) process via possibly re-trapping the newly formed polyselenides.

Ex situ SEM images have been further investigated at different charge–discharge states to clearly monitor the reaction mechanisms of the Se-Cu electrode. As seen in **Figure 7**a, the primary electrode shows a relatively smooth surface. Primary Se and Cu crystals with particle size from 0.5 to 5 μm are well wrapped by Super-P carbons and PTFE binders. SEM image of the electrode discharged to point B (Figure 7b) shows a dramatic morphology change, which composes of large particles and curved short rods (1–3 μm). After the electrode discharged to point D (Figure 7c), it shows middle-range curved wires (4–8 μm) together with large particles with sizes range from 0.5 to 5 μm. When the electrode is fully magnesiated, the predominating morphology (Figure 7d) is a mixture of long-range curved wires (7–12 μm) and particles with relatively low size (less than 1 μm). However, the SEM images at point F (Figure 7e) and point G (Figure 7f) exhibit sheet-like morphology both with small particles, respectively. These results also reveal that the Se-Cu electrodes undergo dramatic morphology and composite changes during the charge–discharge process. These electrode volume changes derived from the decomposition/regeneration of intermediates would negatively influence their long-term cycling performance due to the detachment of the active material from the current collector.

2.4. Identification of Discharge Products of the Cycled Se-Cu Electrode

Identifying the phase structures of wire-like and small particles in the fully discharged products is beneficial to understand this new and reversible reaction mechanism. The STEM images clearly show that the discharged electrode composes of wire-like species together with small particles as shown in **Figure 8**a, which is consistent with SEM images. Elemental mapping (see Figure 8b–f) explicitly reveals that the wire-like species are intensive copper element, indicating the formation of Cu wires. Considering the irregular morphology (large particles) of initial added crude Cu powders, the reformation of Cu wires provides direct evidence for the Cu oxidation and re-deposition on the surface of the electrode. It could also be expected that the reformed Cu nanowires could enhance the electronic conductivity of the cycled electrode, leading to faster reaction kinetics. The smaller particles (see Figure 8be,f) around the Cu wires are mainly composed of Se and Mg elements, confirming the formation of MgSe and $MgSe_2$ phases. The comparison of Mg/Se atomic ratio in Cu-rich and Mg-rich regions (Figure 8g,h) also reveals that smaller particles may be dominate MgSe phases together with partial $Mg_{2x}Cu_3Se_2$ phases.

2.5. Proposed Mg-Ion Storage Mechanisms

Combining the above analysis, we can conclude that the selenium powder can be reduced by at least two steps from Se(0) to Se_n^{2-}, and then to Se_2^{2-} and Se^{2-}, while the Cu metal is oxidized to Cu(I) and Cu(II), most probably forming Cu_3Se_2 crystals as indicated by the XRD results. The fully discharged products compose of dominate MgSe and partial $Mg_{2x}Cu_3Se_2$ nanoparticles as discussed above. When the Se-Cu electrode is fully recharged, metallic Cu wires appear accompanied by the disappearance of MgSe crystals and significantly reduced XRD peak intensity of Cu_3Se_2 particles.

Interestingly, the above structure–composite–properties relationships are analogous to a reversible Cu extrusion–insertion electrode for lithium-ion battery.[34] Tarascon and co-workers explore a fully reversible Li-driven displacement reaction in layered $Cu_{2.33}V_4O_{11}$ electrode,[34] which well coincides with our experiments. Hence, an assumption has been proposed that the transformation of Se into MgSe occurs in a combined intercalation-type and displacement-type reaction with the assistance of

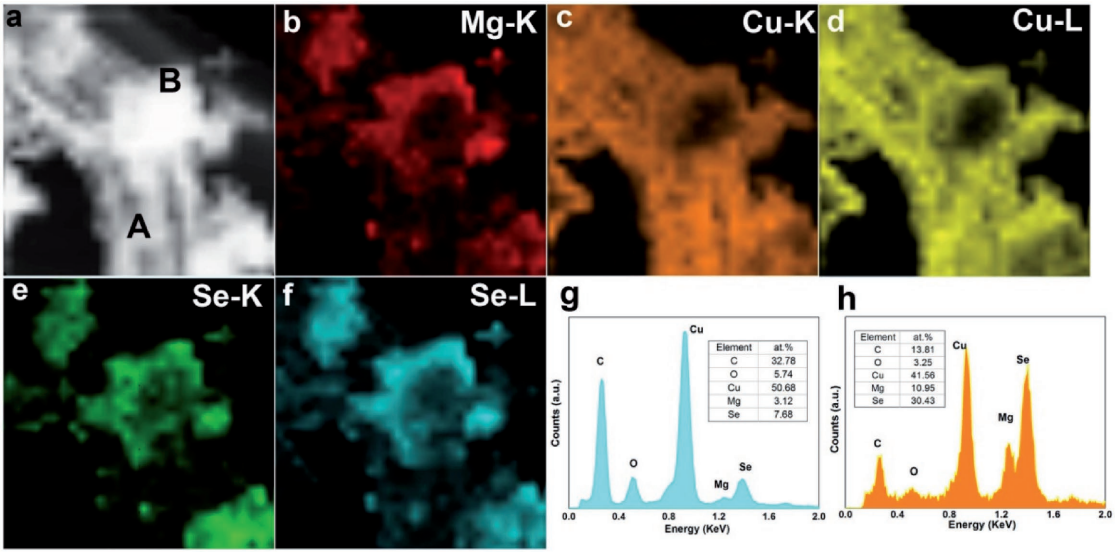

Figure 8. a) STEM images and the corresponding elemental mapping images of the cycled Se-Cu electrode: b) Mg, c,d) Cu, e,f) Se, g) point A in (a), and h) point B in (a).

intermediate phase of Cu_3Se_2 as following equations (also see the comparison working mechanism in **Scheme 1**)

$$Se_8\,(Solid) + 2e^- \leftrightarrow Se_8^{2-}\,(Liquid) \quad (2)$$

$$Se_8^{2-}\,(Liquid) + 12\,Cu\,(Solid) \leftrightarrow 4Cu_3Se_2\,(solid) + 2e^- \quad (3)$$

$$Cu_3Se_2\,(solid) + 2xMg^{2+} + 4xe^- \leftrightarrow Mg_{2x}Cu_3Se_2\,(solid) \quad (0.1 \le x \le 0.5) \quad (4)$$

$$Mg_{2x}Cu_3Se_2\,(solid) \leftrightarrow 3\,Cu\,(solid) + 2(x+1)\,MgSe\,(solid) \quad (0.5 \le x \le 1) \quad (5)$$

$$Se + Mg^{2+} + 2e^- \leftrightarrow MgSe \quad (6)$$

In light of the complicated hypotheses on reaction mechanism, we do an additional XRD survey on the fully charged and discharged states at first, second, and tenth cycles. As seen in **Figure 9**a, the XRD patterns of the second charge–discharge products show similar changes as that of first cycles, indicating

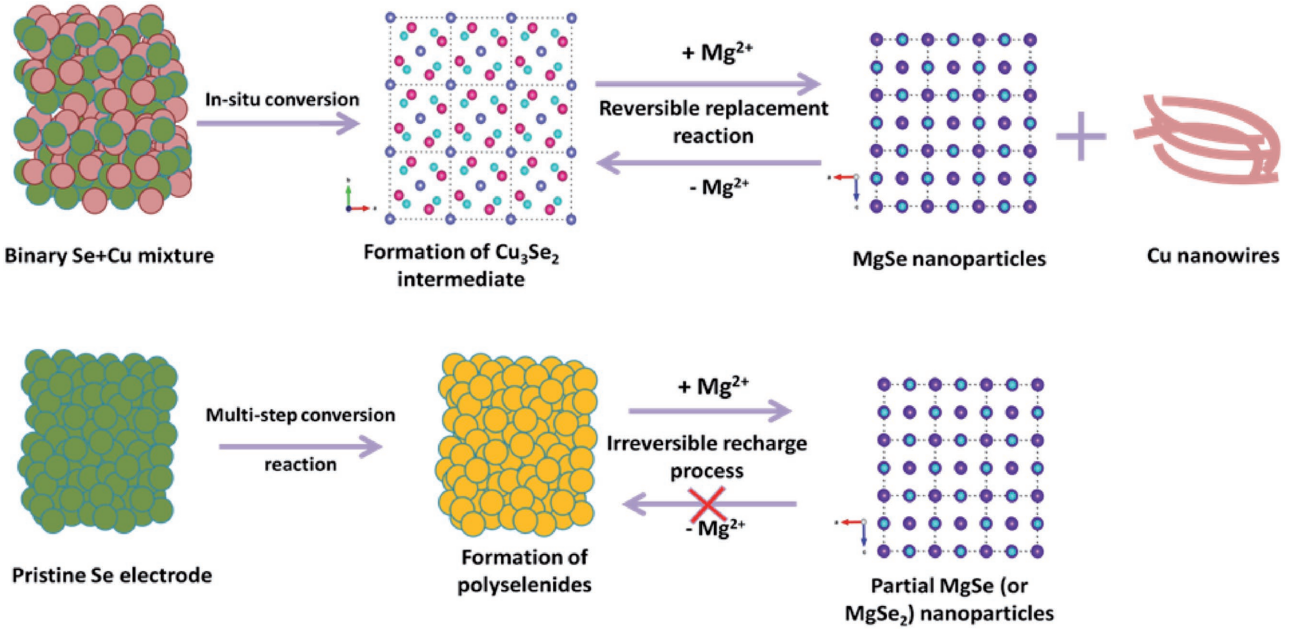

Scheme 1. Working mechanism of the Se-Cu electrode and the pristine Se electrode.

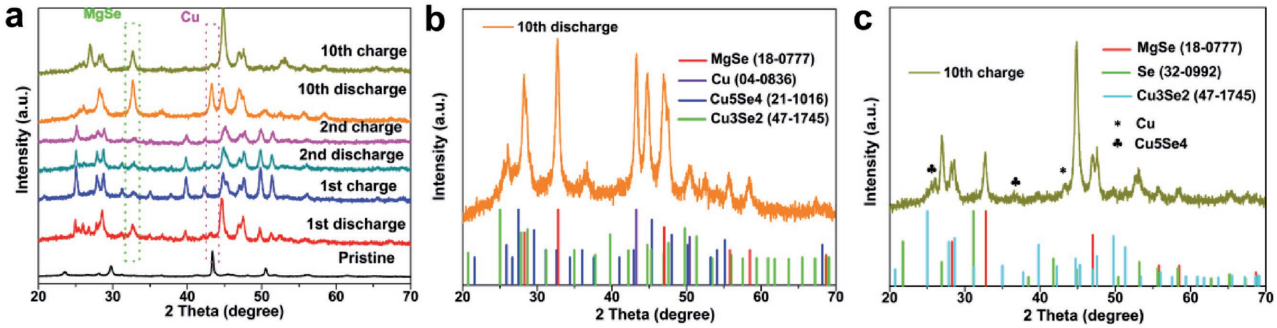

Figure 9. a) XRD patterns of the Se-Cu electrode at fully charged and discharged state at first, second, and tenth cycles; b) XRD pattern of the Se-Cu electrode at fully discharged state at tenth cycle; c) XRD pattern of the Se-Cu electrode at fully charged state at tenth cycle.

the displacement reactions occur in subsequent cycles. More obvious evidence of the displacement reaction has been proved in the XRD patterns of the tenth charge–discharge products. With regard to the tenth discharge products, a mixture of Cu metal and MgSe phase is mainly detected in the XRD patterns together with partial Cu_3Se_2 phases and a trace of $Cu_{2-x}Se$ species (i.e., Cu_5Se_4 phases as seen in Figure 9b). The major peak in Figure 9c at ≈45° and 27° might be ascribed to Berzelianite $Cu_{2-x}Se$ (PDF No. 88-2043) phase. While dominant Cu_3Se_2 phases combined with partial MgSe, crystal Se species, and negligible Cu metals are observed in the XRD patterns in Figure 9c. It should be noted that several side reaction may be concomitantly involved in the given system during the charge–discharge process due to the high activity of high-order polyselenides toward the newly formed Cu wires, for example, the formation of $Cu_{2-x}Se$ species in both charge and discharge products. The generation and disappearance of Cu wires occur in accompany with a highly reversible recrystallization and decomposition of the MgSe discharged particles, further providing strong evidences on the reversible displacement reaction of Equation (5). Hence, the main reaction during the charge–discharge process should be the combined electrochemical intercalation and replacement reactions based on robust Cu_3Se_2 intermediate. The unique reaction pathways induced by Cu powder addition also support the high rate capability of Mg/Se batteries in this work and our previous work.[19]

Based on the aforementioned reaction mechanisms of the Se-Cu electrode, the observed CV peaks (Figure 2b) can be explained accordingly. There are three reduction peaks at 1.1, 0.8, and 0.6 V versus Mg in the first CV cycle (Figure 2b) for the Se-Cu electrode, which might be attributed to the reduction of Se to polyselenides (Se_8^{2-}), the intercalation of Mg-ions into Cu_3Se_2 intermediate phase, and the displacement reaction of the $Mg_{2x}Cu_3Se_2$ phase, respectively. During the recharged process, typical multistep oxidation of MgSe products occurs as demonstrated by Equation (6) or so cathodic peaks in the first CV cycle (Figure 2b). In the second CV cycle, Se-Cu electrode shows two pairs of cathodic and anodic peaks at about 1.2 and 1.5 V versus Mg and 1.2 and 0.8 V versus Mg, which might be ascribed to the intercalation/de-intercalation of Mg-ions into Cu_3Se_2 intermediate phase and the decomposition/re-formation of the $Mg_{2x}Cu_3Se_2$ phase, respectively.

As discussed above, the discharged products of MgSe nanoparticles and Cu nanowires first transform to $Mg_xCu_3Se_2$ and then to Cu_3Se_2 during each recharged processes. When all copper are depleted to form Cu_3Se_2, the residual MgSe can hardly transform to Se or Cu_3Se_2 intermediate due to its intrinsic sluggish recharge reactions. The nonstoichiometry of Se-Cu electrode (with weight ratio of 1:1) for the formation of Cu_3Se_2 intermediate might result in a mixture of Cu_3Se_2 with a small amount of MgSe after each charged cycle in the actual cathodes. The stoichiometry of Se-Cu electrode (with weight ratio of 1:1.2) for the formation of Cu_3Se_2 intermediate has also been tested as reference system as seen in Figure S13 (Supporting Information). Compared to the Se-Cu electrode with Se/Cu weight ratios higher than 1:1.2, the stoichiometry of Se-Cu electrode displays higher specific capacity (based on the weight of Se) and longer voltage plateau at 1.0 V versus Mg. However, it displays lower specific capacity (not only based on weight of Se but also based on the total mass of Se and Cu) and Coulombic efficiency than that of Se-Cu electrode with Se/Cu weight ratios of 1:2 when they reach their optimized conditions. All these results indicate that the introduction of excess copper is indeed beneficial to the electrochemical kinetics and the electrochemical properties of the Se-Cu electrode.

With higher copper content, Se-Cu electrodes display longer voltage plateau at 1.0 V versus Mg as seen in Figure S4b (Supporting Information). It is easy to speculate that the introduction of copper and its high reactivity toward polyselenides species induce the formation of Cu_3Se_2 intermediate, which changes the magnesiation/demagnesiation pathways of Se electrode. Higher copper contents contribute to more chances to form the Cu_3Se_2 intermediate, which results in much more complete displacement reaction at a lower voltage plateau of 1.0 V versus Mg, while insufficient copper contents may cause partial Se remaining in the cathode which directly transforms to MgSe at higher voltage plateau of 1.2–1.4 V versus Mg.

In addition, pure phase of Cu_3Se_2 has been synthesized by facile high-energy ball milling process and their electrochemical performances have been characterized as shown in Figure S14 (Supporting Information). XRD pattern indicates a pure phase of Cu_3Se_2 without impurity peaks and typical TEM image reveals its granular morphology with average length of 1.5 μm. Figure S14c (Supporting Information) depicts its 31st galvanostatic charge/discharge profile, which shows a specific capacity of 82 mAh g^{-1}, much lower than that of the Se-Cu electrodes. The corresponding cycling performance of the pure phase Cu_3Se_2 reveals that it needs more conditioning cycles to

reach their optimized capacity. Changing Mg-ion electrolytes without electrolytic conditioning processes and down-sizing the Cu_3Se_2 particles might be ideal strategies to improve its magnesiation/demagnesiation kinetics. These results also demonstrate Cu_3Se_2 might be a promising cathode for Mg-ion batteries.

3. Conclusion

In this work, the Se-Cu binary system is studied to show dramatic enhancements in terms of the cell reversibility and cycling stability compared to that of the pristine Se electrode. Several analysis techniques including ex situ XRD, SEM, and XPS tests reveal that the initially formed Cu_3Se_2 intermediate induces an unconventional yet reversible process occurring in two-stage magnesiation mechanism: during the first stage, this thermodynamically stable phase participates in the Mg-ion intercalation reaction up to the composition range of $0.1 \leq x \leq 0.5$ in $Mg_{2x}Cu_3Se_2$, beyond which the conversion (displacement type) reaction takes place to generate Cu nanowires and MgSe nanoparticles. In sharp comparison with the pristine Se electrode, the binary Se-Cu electrode shows an average specific capacity of 365 mAh g^{-1} at a current density of 10 mA g^{-1} and remains 71.7% capacity retention for more than 100 cycles. To our best knowledge, this system is the first implementation of microsized Se-based cathode for secondary Mg batteries. More bracingly, Se/C nanostructures fabricated by facile blade coating Se nanorodes onto copper foils exhibit high output power and capacity (696.0 mAh g^{-1} at 67.9 mA g^{-1}), which outperforms all previously reported Mg/Se batteries. Self-established rapid magnesiation/de-magnesiation pathway revealed by our work may represent a new solution to achieve better electrochemical activity, high rate capability, and long-term durability of selenium (sulfur) electrode for the development of high energy density Mg batteries.

4. Experimental Section

Synthesis of BCM Electrolyte: The synthetic procedures of electrolytes (BCM electrolyte) were carried out within an Ar-filled glove box (Mikrouna) with H_2O and O_2 concentrations less than 0.1 ppm. The BCM electrolyte is prepared by facile dissolution of both THFPB (tris(2H-hexafluoroisopropyl) borate, 95%, TCI (Shanghai)), and anhydrous magnesium fluoride (MgF_2, 99.99%, J&K Chemical Ltd. (Shanghai)) into 1,2-dimethoxyethane (DME) solutions. In a typical procedure, 0.2048 g THFPB was carefully dissolved into 4 mL anhydrous DME followed by adding 0.0124 g MgF_2, which was vigorously stirred for at least 20 min prior to use. The preparations of varied electrolytes including APC, MACC, and HMDS are referred in previous literatures.

Characterizations of Both Electrodes: The surface morphology of the cycled pristine Se electrode and the Se-Cu electrode was characterized by using a field-emission scanning electron microscopy (FE-SEM, JSM 6700F) operating at 10 kV. The phase compositions of the pristine Se electrode and the Se-Cu electrode were investigated by XRD (Rigaku D-max-γA with Cu Kα radiation). First, the cell was detached into several components and it was found that the electrode films were separated from the SS electrode, which preserved a similar circular shape. The electrodes were carefully removed from glass fiber and washed with anhydrous DME solutions for several times prior to testing. XPS analysis was performed on a Perkin-Elmer PHI 550 spectrometer with Al Kα (1486.6 eV) as the X-ray source. The morphology of discharged electrodes and their corresponding element distributions were further characterized by STEM images and STEM-EDS mappings.

DFT Calculations: The first principles calculations were performed to acquire the mechanism of magnesium inserting in the Cu_3Se_2 anode materials based on the DFT. In this modeling, the unit cell of Cu_3Se_2 has the space group of P-421m. In the calculation used in this study, the Perdew–Burke–Ernzerhof (PBE) was chosen to describe the electron exchange within the generalized gradient approximation (GGA) using the Vienna ab initio Simulation Package (VASP),[35,36] and the cutoff energy of 520 eV was set with a $4 \times 4 \times 4$ Monkhorst–Pack *k*-point mesh. Herein, the full relaxation was completed when the force convergence criterion was less than 0.05 eV $Å^{-1}$, and the total energies convergence criterion is below 10^{-5} eV in all the calculations. After the structure optimized, the lattice parameters for the Cu_3Se_2 unit cell are $a = 6.393$ Å, and $c = 4.311$ Å, in agreement with the experimental results.[37]

Electrode Fabrications and Electrochemical Measurements: For the fabrication of the pristine Se electrode, commercially available Se powders, super-P, and PTFE were mixed together at a weight ratio of 70:20:10 within ethanol to form homogeneous mixture. And then the mixture was rolled and pressed into a self-supported electrode and then dried at 120 °C to evaporate solvent to access the pristine Se electrode. The electrode was tailored into proper size with an average area of ≈1.0 cm^2 and the mass loading of the active Se was estimated to be 4.0 mg cm^{-2} via weighing the loaded electrode. For the fabrication of the Se-Cu electrode, a mixture of Se powder, Cu powder, Super-P, and PTFE was mixed together at weight ratio of 40:40:10:10 within the same solvent to prepare the Se-Cu electrode. The electrode was tailored into proper size with an average area of ≈1.0 cm^2 and the mass weight of the Se-Cu composites was also estimated to be ≈4.0 mg cm^{-2}. The pre-tailored Mg foil was used as anode and the as-prepared BCM solution containing 0.05 M MgF_2 and 0.1 M THFPB in DME was served as Mg-ion electrolyte. The typical CR2032-type coin cell was assembled within an Ar-filled glove box (Mikrouna) with moisture and oxygen concentrations less than 0.1 ppm. The reaction mechanisms of both electrodes in BCM electrolyte were investigated via CV tests using electrochemical workstation (ZAHNER-Elektrik GmbH & Co. KG, Germany). The scan potential was controlled within a voltage range of 0.4–2.1 V versus Mg with a scan rate of 0.05 mV s^{-1}. The charge–discharge properties of both electrodes were studied by galvanostatic discharge–charge experiments within a potential between 0.4 and 2.1 V versus Mg at a constant current density of 10 mA g^{-1}.

Supporting Information

Supporting Information is available from the Wiley Online Library or from the author.

Acknowledgements

Z.Z. and B.C. contributed equally to this work. This work was supported by the National Science Fund for Distinguished Young Scholars (51625204), the National Natural Science Foundation of China (51502319), and the Shandong Provincial Natural Science Foundation (No. ZR2016BQ18).

Conflict of Interest

The authors declare no conflict of interest.

Keywords

displacement reactions, high reversibility, intercalation reactions, magnesium batteries, selenium cathodes

Received: March 31, 2017
Revised: September 14, 2017
Published online:

[1] J. Muldoon, C. B. Bucur, T. Gregory, *Chem. Rev.* **2014**, *114*, 11683.
[2] P. Saha, M. K. Datta, O. I. Velikokhatnyi, A. Manivannan, D. Alman, P. N. Kumta, *Prog. Mater. Sci.* **2014**, *66*, 1.
[3] J. Muldoon, C. B. Bucur, A. G. Oliver, T. Sugimoto, M. Matsui, H. S. Kim, G. D. Allred, J. Zajicek, Y. Kotani, *Energy Environ. Sci.* **2012**, *5*, 5941.
[4] D. Aurbach, Z. Lu, A. Schechter, Y. Gofer, H. Gizbar, R. Turgeman, Y. Cohen, M. Moshkovich, E. Levi, *Nature* **2000**, *407*, 724.
[5] T. Gao, M. Noked, A. J. Pearse, E. Gillette, X. Fan, Y. Zhu, C. Luo, L. Suo, M. A. Schroeder, K. Xu, S. B. Lee, G. W. Rubloff, C. Wang, *J. Am. Chem. Soc.* **2015**, *137*, 12388.
[6] C. P. Yang, Y. X. Yin, Y. G. Guo, *J. Phys. Chem. Lett.* **2015**, *6*, 256.
[7] W. F. Li, S. Cheng, J. Wang, Y. C. Qiu, Z. Z. Zheng, H. Z. Lin, S. Nanda, Q. Ma, Y. Xu, F. M. Ye, M. N. Liu, L. S. Zhou, Y. G. Zhang, *Angew. Chem., Int. Ed.* **2016**, *55*, 6406.
[8] Z. Zhao-Karger, X.-M. Lin, C. B. Minella, D. Wang, T. Diemant, R. J. Behm, M. Fichtner, *J. Power Sources* **2016**, *323*, 213.
[9] Z. Zhao-Karger, X. Y. Zhao, D. Wang, T. Diemant, R. J. Behm, M. Fichtner, *Adv. Energy Mater.* **2015**, *5*, 9.
[10] X. Yu, A. Manthiram, *ACS Energy Lett.* **2016**, *1*, 431.
[11] Y. Koyama, Y. Yamada, I. Tanaka, S. R. Nishitani, H. Adachi, M. Murayama, R. Kanno, *Mater. Trans.* **2002**, *43*, 1460.
[12] S. W. Oh, S.-T. Myung, H. J. Bang, C. S. Yoon, K. Amine, Y.-K. Sun, *Electrochem. Solid State Lett.* **2009**, *12*, A181.
[13] X. M. Lou, Y. X. Zhang, *J. Mater. Chem.* **2011**, *21*, 4156.
[14] X. Sun, P. Bonnick, L. F. Nazar, *ACS Energy Lett.* **2016**, *1*, 297.
[15] X. Sun, P. Bonnick, V. Duffort, M. Liu, Z. Rong, K. A. Persson, G. Ceder, L. F. Nazar, *Energy Environ. Sci.* **2016**, *9*, 2273.
[16] V. Duffort, X. Sun, L. F. Nazar, *Chem. Commun.* **2016**, *52*, 12458.
[17] Y. Tashiro, K. Taniguchi, H. Miyasaka, *Electrochim. Acta* **2016**, *210*, 655.
[18] S.-H. Choi, J.-S. Kim, S.-G. Woo, W. Cho, S. Y. Choi, J. Choi, K.-T. Lee, M.-S. Park, Y.-J. Kim, *ACS Appl. Mater. Interfaces* **2015**, *7*, 7016.
[19] Z. Zhang, Z. Cui, L. Qiao, J. Guan, H. Xu, X. Wang, P. Hu, H. Du, S. Li, X. Zhou, S. Dong, Z. Liu, G. Cui, L. Chen, *Adv. Energy Mater.* **2017**, *7*, 1602055.
[20] Y. Diao, K. Xie, S. Xiong, X. Hong, *J. Electrochem. Soc.* **2012**, *159*, A421.
[21] H. S. Kim, T. S. Arthur, G. D. Allred, J. Zajicek, J. G. Newman, A. E. Rodnyansky, A. G. Oliver, W. C. Boggess, J. Muldoon, *Nat. Commun.* **2011**, *2*, 427.
[22] F. Wu, J. T. Lee, Y. Xiao, G. Yushin, *Nano Energy* **2016**, *27*, 238.
[23] A. Abouimrane, D. Dambournet, K. W. Chapman, P. J. Chupas, W. Weng, K. Amine, *J. Am. Chem. Soc.* **2012**, *134*, 4505.
[24] N. S. Hartig, P. K. Dorhout, S. M. Miller, *J. Solid State Chem.* **1994**, *113*, 88.
[25] F. Hergert, S. Jost, R. Hock, M. Purwins, J. Palm, *Thin Solid Films* **2006**, *511*, 147.
[26] X. Zhou, P. Gao, S. Sun, D. Bao, Y. Wang, X. Li, T. Wu, Y. Chen, P. Yang, *Chem. Mater.* **2015**, *27*, 6730.
[27] N. Martensson, B. Reihl, O. Vogt, *Phys. Rev. B* **1982**, *25*, 824.
[28] R. Golovchak, A. Kovalskiy, O. Shpotyuk, H. Jain, *Solid State Commun.* **2013**, *165*, 22.
[29] A. Ouchi, Z. Bastl, J. Bohacek, H. Orita, K. Miyazaki, S. Miyashita, P. Bezdicka, J. Pola, *Chem. Mater.* **2004**, *16*, 3439.
[30] X. Yu, A. Manthiram, *ACS Energy Lett.* **2016**, 431.
[31] M. I. Diez-Garcia, T. Lana-Villarreal, R. Gomez, *ChemSusChem* **2016**, *9*, 1504.
[32] W. J. Lee, Y. S. Lee, S. K. Rha, Y. J. Lee, K. Y. Lim, Y. D. Chung, C. N. Whang, *Appl. Surf. Sci.* **2003**, *205*, 128.
[33] C. Gabler, C. Tomastik, J. Brenner, L. Pisarova, N. Doerr, G. Allmaier, *Green Chem.* **2011**, *13*, 2869.
[34] M. Morcrette, P. Rozier, L. Dupont, E. Mugnier, L. Sannier, J. Galy, J. M. Tarascon, *Nat. Mater.* **2003**, *2*, 755.
[35] G. Kresse, J. Furthmüller, *Phys. Rev. B* **1996**, *54*, 11169.
[36] G. Kresse, D. Joubert, *Phys. Rev. B* **1999**, *59*, 1758.
[37] N. Morimoto, K. Koto, *Science* **1966**, *152*, 345.

